Journal of Membrane Science 423-424 (2012) 332–341

Contents lists available at SciVerse ScienceDirect

Journal of Membrane Science

journal homepage: www.elsevier.com/locate/memsci

Role of alloying elements in vanadium-based binary alloy membranes for hydrogen separation

Young-Su Lee [a,*], Chuying Ouyang [b], Jin-Yoo Suh [a], Eric Fleury [a], Young Whan Cho [a], Jae-Hyeok Shim [a]

[a] High Temperature Energy Materials Research Center, Korea Institute of Science and Technology, Seoul 136-791, Republic of Korea
[b] Department of Physics, Jiangxi Normal University, Nanchang 330022, People's Republic of China

ARTICLE INFO

Article history:
Received 29 March 2012
Received in revised form
20 July 2012
Accepted 17 August 2012
Available online 27 August 2012

Keywords:
Hydrogen separation membrane
Vanadium alloy
Hydrogen solubility
First-principles calculation

ABSTRACT

We investigate the metal–hydrogen interaction in vanadium alloyed with X=Fe, Ni, Al, Ti, and Nb using first-principles calculations. The site energy of interstitial hydrogen depends on both the volume and the presence of a nearby alloying element; the two effects are analyzed separately. The effective volume of the alloying element follows the sequence Nb > Ti > Al > V > Ni > Fe, and a larger volume lowers the site energy on average. Locally, Al appears to be the strongest hydrogen repellent, and Ti exhibits the strongest affinity for hydrogen. The original tetrahedral coordination by the metal atoms is also affected and the effect is the most pronounced in Ni, where the hydrogen atom in the octahedral interstitial site is strongly stabilized. A 16-atom body centered cubic special quasi-random structure is utilized to obtain the statistical distribution of site energies in $V_{12}X_4$. The obtained site energies at 673 K have the following sequence: Ti < Nb < Al < Ni < Fe. This result indicates that the strongest local repulsion brought by Al is not necessarily correlated to the largest drop in solubility due to the compensation by the elastic effect. The strong repulsion, however, would cause a pronounced decrease in the configurational entropy.

1. Introduction

Increasing demand for renewable and sustainable energy has increased the interest in the use of hydrogen as a clean energy carrier, which is one of the key elements in the carbon-neutral energy cycle. The current production of hydrogen primarily relies on the steam reforming of natural gas, and therefore, subsequent purification is required. Among the available purification methods, the use of dense metallic membranes ensures the best selectivity because hydrogen can exclusively diffuse through the membrane in its atomic form. Palladium alloys, such as Pd–Cu or Pd–Ag, are representatives of these metallic membranes. However, these palladium alloy membranes are plagued by high cost. A cheaper alternative can be group V elements—V, Nb, and Ta. The hydrogen permeability of these elements is greater than that of Pd, but their embrittlement upon exposure to hydrogen has been a serious problem [1,2]. Therefore, an improvement in durability is a prerequisite for the group V alloys to replace Pd alloys.

Several experimental studies have demonstrated that the durability of vanadium can be improved by alloying with Ni, Al, Pd, etc. [3–5]. There could be several interrelated reasons for this improvement in durability, but the most obvious reason is the decrease in solubility upon alloying. At a given temperature and partial pressure of hydrogen, a reduced amount of hydrogen in the material would naturally result in a lesser degree of hydrogen-induced damage. However, this alloying strategy compromises the permeability because permeability is proportional to solubility. Therefore, the objective is to determine the optimum composition that enhances the durability without sacrificing too much permeability. In this regard, understanding and predicting the interactions between hydrogen and the alloying element is essential for designing hydrogen separation membranes.

Permeability, solubility, or diffusivity measurements would provide insight about the characteristic effects of alloying [6–8]. However, the interpretation of these measurements is not straightforward. The hydrogen solution energy (or site energy) of alloys or compounds cannot be easily interpolated from those of the constituent members. For example, the equilibrium hydrogen partial pressure of V alloys at fixed hydrogen to metal atomic ratios (H/M) monotonically increases as 3*d*-elements of higher atomic number are alloyed [9], whereas pure Ni shows a stronger affinity for hydrogen compared to pure Fe. Although both Zr and Pd form hydrides, compounds composed of Zr and Pd can be a very weak hydride former depending on the Zr to Pd ratio [10]. Electronic structure analysis is essential for gaining a fundamental understanding on such issues. The equilibrium partial pressure of hydrogen as a function of H/M [11,12] or the enthalpy

* Corresponding author. Tel.: +82 2 958 5412; fax: +82 2 958 5449.
E-mail addresses: lee0su@kist.re.kr (Y.-S. Lee), cyouyang@jxnu.edu.cn (C. Ouyang), jinyoo@kist.re.kr (J.-Y. Suh), efleury@kist.re.kr (E. Fleury), oze@kist.re.kr (Y.W. Cho), jhshim@kist.re.kr (J.-H. Shim).

0376-7388/$ - see front matter © 2012 Elsevier B.V. All rights reserved.
http://dx.doi.org/10.1016/j.memsci.2012.08.034

change upon hydrogen insertion can be measured experimentally [13]. The preferred interstitial site for hydrogen occupation can be identified based on the vibrational frequencies of interstitial hydrogen [14]. Extensive research has been conducted to correlate these experimentally derived quantities to electronic structure, site energy distribution and site occupation, and even to the role of alloying elements at the atomistic scale [15–18]. Recent advancements in first-principles simulations provide us with more direct access to the atomistic picture without implicit derivation from macroscopically averaged experimental quantities. The predictive power of density functional theory (DFT) calculations reaches such a level as to estimate permeability solely from calculation [19]. Although Pd alloys have been extensively studied using DFT calculations [19–23], very little research has been performed with vanadium alloys toward understanding the role of alloying elements in view of the electronic structure [24]. Here, we investigate the V–X alloy systems where X=Ti, Fe, Ni, Al, and Nb. Ti, Fe, and Ni were chosen to determine the systematic variation in the 3*d* transition metal series. Al was chosen as a typical alloying element that is not a transition metal, and Nb represents an element that belongs to the same group. We explore several factors, such as elastic and electronic effects, that could affect the site energies. The coordination environment of hydrogen and site blocking are also analyzed.

2. Calculations

We perform DFT calculations using the exchange-correlation functional by Perdew–Burke–Ernzerhof [25] with the Quantum-ESPRESSO software package [26]. The cutoff energy for the planewave and charge density are set to 40 and 400 Ry, respectively. A regular *k*-point mesh of $12\times12\times12$ with a smearing of 0.02 Ry is used for the body centered cubic unit cell, and the same sampling density is applied to the supercells.

To calculate the site energy for hydrogen insertion into V alloys, a $3\times3\times3$ supercell containing 54 metal atoms is used. The symmetry of the alloy supercell for $V_{53}X_1$, $V_{52}X_2$, $V_{48}X_6$, and $V_{42}X_{12}$ is restricted to *Pm*-3*m* to limit the number of symmetrically independent sites. Within this symmetry, there are 12 independent tetrahedral interstitial sites for H atoms. Tables 1 and 2 summarize the positions of the X atoms and the H atoms, respectively. For a better description, we graphically illustrate the H positions in Fig. S1 and present a schematic diagram of the connectivity between different H positions in Fig. S2. To obtain the site energy distribution without the use of an artificial symmetry, we adopt a special quasi-random structure (SQS) of the bcc alloy for $V_{12}X_4$ at high X concentrations [27]. All of the calculations were performed in spin-unpolarized conditions. Spin polarized calculations were performed for the Fe and Ni substitutions, but non-magnetic ground states were obtained.

3. Results and discussion

3.1. Elastic effect

Here, the hydrogen site energy is defined as the total energy change upon the insertion of hydrogen into the metal matrix, as in Eq. (1). The zero point energy and finite temperature effect are not considered because we focus on the difference between each alloying element rather than extracting accurate absolute site energies from first-principles calculations.

$$\Delta E = E(V_{m-n}X_nH) - E(V_{m-n}X_n) - (1/2)E(H_2) \quad (1)$$

According to literature, the site energy is a function of H/M; it initially decreases (becomes more exothermic) as H/M increases, and then it increases after reaching the minimum [12,15,28,29]. This behavior is a general feature that is irrespective of the constituent metal elements. The increase in energy, i.e., the insertion of hydrogen becoming less favorable, originates from a direct repulsion among the H atoms or an occupation of the anti-bonding states by the added electrons. However, the initial decrease in energy is largely due to elastic effects. The site energy or enthalpy change as a function of the hydrogen concentration can be decomposed into two parts at constant temperature [29]:

$$\frac{d\,\Delta\overline{H}_H}{dc} = \left(\frac{\partial\,\Delta\overline{H}_H}{\partial\ln V}\right)_c\left(\frac{\partial\ln V}{\partial c}\right) + \left(\frac{\partial\,\Delta\overline{H}_H}{\partial c}\right)_V \quad (2)$$

The first term on the right hand side refers to the dependence of the enthalpy change on the volume at fixed concentration, and can be written as follows [15]:

$$\left(\frac{\partial\,\Delta\overline{H}_H}{\partial\ln V}\right)_{c,T} = -B\overline{V}_H + BT\left(\frac{\partial\overline{V}_H}{\partial T}\right)_P, \quad (3)$$

where B and $\overline{V}_H$ are the bulk modulus and partial molar volume of hydrogen, respectively. Neglecting the temperature dependence of $\overline{V}_H$ (the second term on the right hand side), the remaining terms can be determined using DFT calculations at a 0 K limit by replacing the enthalpy change with the total energy change, as in Eq. (1). Fig. 1 shows the ΔE as a function of $\ln(V/V_o)$ for the insertion of a single hydrogen atom into the 54-atom V supercell. This relationship varies almost linearly in the volume range of $\pm2\%$, and the slope is -3.19 eV, which is the left hand side in Eq. (3). The calculated bulk modulus of pure V (185.3 GPa) and the volume of hydrogen (2.65 Å^3/atom) from variable cell relaxations compare well with experimental values [30–32], and their multiplication, $B\overline{V}_H$, is 3.06 eV. The good agreement between the two approaches indicates that both the hydrogen concentration and the volume change are small enough that the elastic effect remains close to that of pure vanadium.

Table 1
Alloy compositions and the position of the alloying elements.

	x_X	Wyckoff position	Coordinates
$V_{53}X_1$	0.0185	1*b*	(1/2, 1/2, 1/2)
$V_{52}X_2$	0.0370	1*b*, 1*a*	(1/2, 1/2, 1/2), (0, 0, 0)
$V_{48}X_6$	0.1111	6*f*	(1/6, 1/2, 1/2),
$V_{42}X_{12}$	0.2222	12*j*	(1/6, 1/6, 1/2)

Table 2
Twelve independent H positions in the 54-atom simulation cell with $Pm-3m$ symmetry. The positions are sorted in ascending order of d_{Hb}-d_{Ha}. The last column shows four nearest neighbor *T* sites; the number in front of the position index is the multiplicity.

	Wyckoff position	Coordinates	Distance from 1*b* (d_{Hb} in Å)	Distance from 1*a* (d_{Ha} in Å)	Neighboring *T* sites
H1	24*l*	(1/3, 5/12, 1/2)	1.675	6.574	3H1, H2
H2	24*l*	(1/4, 1/3, 1/2)	2.701	5.851	H1, H2, 2H3
H3	48*n*	(1/6, 1/3, 5/12)	3.433	5.025	H2, H3, H4, H6
H4	24*l*	(1/12, 1/3, 1/2)	4.034	5.454	2H3, H5, H7
H5	12*h*	(0, 5/12, 1/2)	4.557	5.851	2H4, 2H5
H6	48*n*	(1/6, 1/4, 1/3)	4.034	4.034	H3, 2H6, H10
H7	12*h*	(0, 1/4, 1/2)	5.025	5.025	2H4, 2H9
H8	12*h*	(0, 1/12, 1/2)	5.851	4.557	2H8, 2H9
H9	24*k*	(0, 1/6, 5/12)	5.454	4.034	H7, H8, 2H10
H10	48*n*	(1/12, 1/6, 1/3)	5.025	3.433	H6, H9, H10, H11
H11	24*k*	(0, 1/6, 1/4)	5.851	2.701	2H10, H11, H12
H12	24*k*	(0, 1/12, 1/6)	6.574	1.675	H11, 3H12

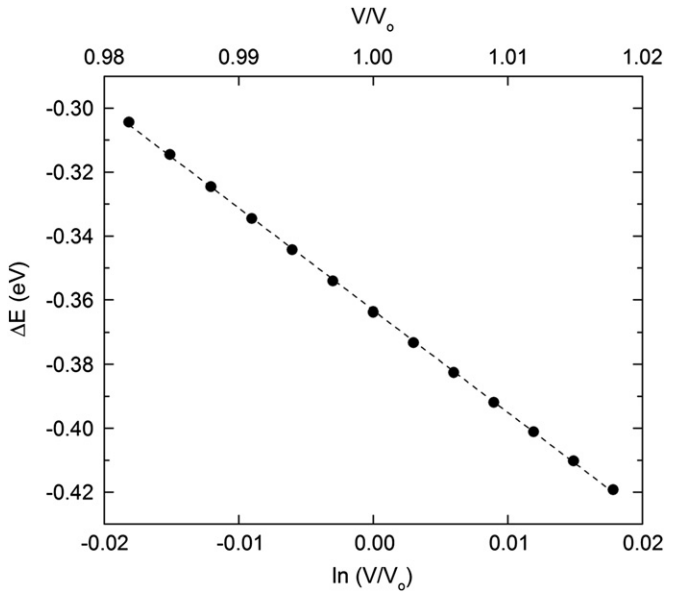

Fig. 1. Site energy as a function of volume. The volume is isotropically varied.

The obtained elastic effect is quite sizeable: even a 1% change in volume could cause a change as large as ~30 meV in the site energy. The fact that the enthalpy change decreases until H/V reaches ca. 0.3 in pure vanadium [11,12] hints at such an important contribution. The reason why we highlight the elastic effect is that, in alloys, the elastic effect always coexists with the electronic effect. Note that Eq. (3) originally concerns the volume change resulting from the addition of hydrogen, but the concept can be extended to the volume change caused by alloying. Fig. S3 presents calculated lattice parameters upon substituting Fe, Ni, Al, Ti, or Nb for V. In general, the lattice parameter varies linearly with the alloy concentration (x_X), and it follows the sequence Nb > Ti > Al > V > Ni > Fe. If the elastic effect plays the primary role, Fe would increase ΔE the most, whereas Nb would decrease it the most. In the next section, we analyze the ΔE of V-alloys in low alloying concentrations ($x_X < 0.05$) considering the elastic effect.

3.2. Low alloy concentration

3.2.1. Elastic effect

The elastic effect can be examined in both the averaged manner and in the local level. Globally, ΔE can be simply estimated from the total cell volume of the alloys based on the relationship shown in Fig. 1. Locally, each symmetrically independent H site will have a different available volume. The volume of the tetrahedron composed of four metal atoms is calculated for 12 H positions in the relaxed $V_{53}X_1$ or $V_{52}X_2$ geometry. Then, the H atom is placed at each position and the atomic positions are optimized without any symmetry restriction to obtain the site energies. The results are plotted in Fig. 2. The site energies are apparently strongly affected by the volume of the tetrahedron. Both ΔE and the volume of the tetrahedron converge to the globally estimated values (solid lines) as the distance from the X atom increases; the convergence is the fastest in Fe and the slowest in Al, where even the H12 position appears to be not far enough. Among the metals examined, Ti is the only one that exhibits strong short-range attraction. The site energy at H1 (V_3Ti_1 site, where the notation V_nX_{4-n} is used for a tetrahedral site coordinated by n V atoms and $(4-n)$ X atoms) is 48 meV lower than the estimated value. Al is the strongest hydrogen repellent. Hydrogen cannot even sit next to Al: it spontaneously falls into the neighboring H2 site. In addition, the site energy remains above the estimated value irrespective of the tetrahedron volume at each site.

The behavior in the V–Nb system is also noteworthy. Although hydrogen insertion occurs more exothermically in pure Nb than in pure V [15], Nb does not attract hydrogen when it is inside the V matrix. It was reported that the V_3Nb_1 site would have higher energy than the V_4 site in all compositions of the V–Nb alloy due to the larger size of Nb and the resultant smaller effective interstitial site [15]. However, the next nearest H2 site is the one that benefits from the large Nb; it has the maximum tetrahedron volume and the minimum site energy. From the site energy profile, we can infer that Nb would form an increased H population around it, though not at its immediate neighboring interstitial sites.

In the case of the $V_{52}X_2$ structure, which has one more X atom at the origin, the variation in the site energy appears similar. However, the X–X distance appears sufficiently close or x_X appears sufficiently high that the convergence of the site energy to the estimated value (dashed line) could not be achieved. In addition, the estimated value itself becomes inaccurate as x_X increases because it is extrapolated from the pure V data.

3.2.2. Electronic effect

Upto this point, we have primarily discussed the elastic effect, and now we attempt to isolate the electronic contribution. The ΔE vs. $\ln(V/V_o)$ plot in Fig. 1 can serve as a baseline for the underlying elastic effect. When the site energies are overlaid on the same graph, the deviation, not the absolute value, from this baseline would correspond to the electronic contribution. The solid symbols in Fig. 2f are the weighted (by the total number of equivalent sites) average of the site energies against the weighted average of $\ln(V/V_o)$, where V is the tetrahedron volume at each interstitial site and V_o is that of pure V. Note that the case of Al is ill-defined because the H1 site (and the H12 site in $V_{52}X_2$) is unstable, and here, the average site energy excluding those unstable sites is considered (the data points are placed inside parentheses). The interpretation is now straightforward; if the absolute values are compared in the case of $V_{53}X_1$, the sequence is Ti < Nb < Fe < (Al) < Ni, but the order changes to Ti < Fe < Nb < Ni < (Al) if the deviation from the baseline is considered. Based on this analysis, one may reason that the elastic effect would primarily account for the lower site energy in Nb compared to that in Fe, and preference for Ti over Nb, or Fe over Ni, is certainly due to the electronic effect.

Although the tetrahedron volume is a good measure of the available space for the H atom, the effective open space certainly depends on the relative positions and the types of metal atoms, even at the same tetrahedron volume. For example, when X is large, the tetrahedron volume of the V_3X_1 site is likely to be larger than that of the V_4 site, but a large X atom will reduce the effective open space for the H atom. This result might be the reason why even Ti, which strongly attracts H, exhibits a positive deviation from the elastic baseline. To compare all of the alloying elements on equal footing, we calculate the average ΔE and $\ln(V/V_o)$ of the V_4 sites and present them as open symbols in Fig. 2f. As expected, the deviation of large alloying elements (Al, Ti and Nb) becomes smaller in general. The sequence in the absolute ΔE is the same as what we observed in the total average (Ti < Nb < Fe < Al < Ni), but the sequence in the deviation is changed to favor Nb over Fe (Ti < Nb < Fe < Ni < Al). Two clear trends arise from the electronic contribution: first, the sequence among the 3*d* transition metal elements, Ti < Fe < Ni, is always preserved, and second, Al increases ΔE the most significantly, both locally and globally. In fact, the strongest repulsion by Al might not be readily observed if the absolute ΔE values are contrasted. To understand the origin of the electronic contribution, we now move to the case of higher alloy concentrations where the electronic effect would become more evident.

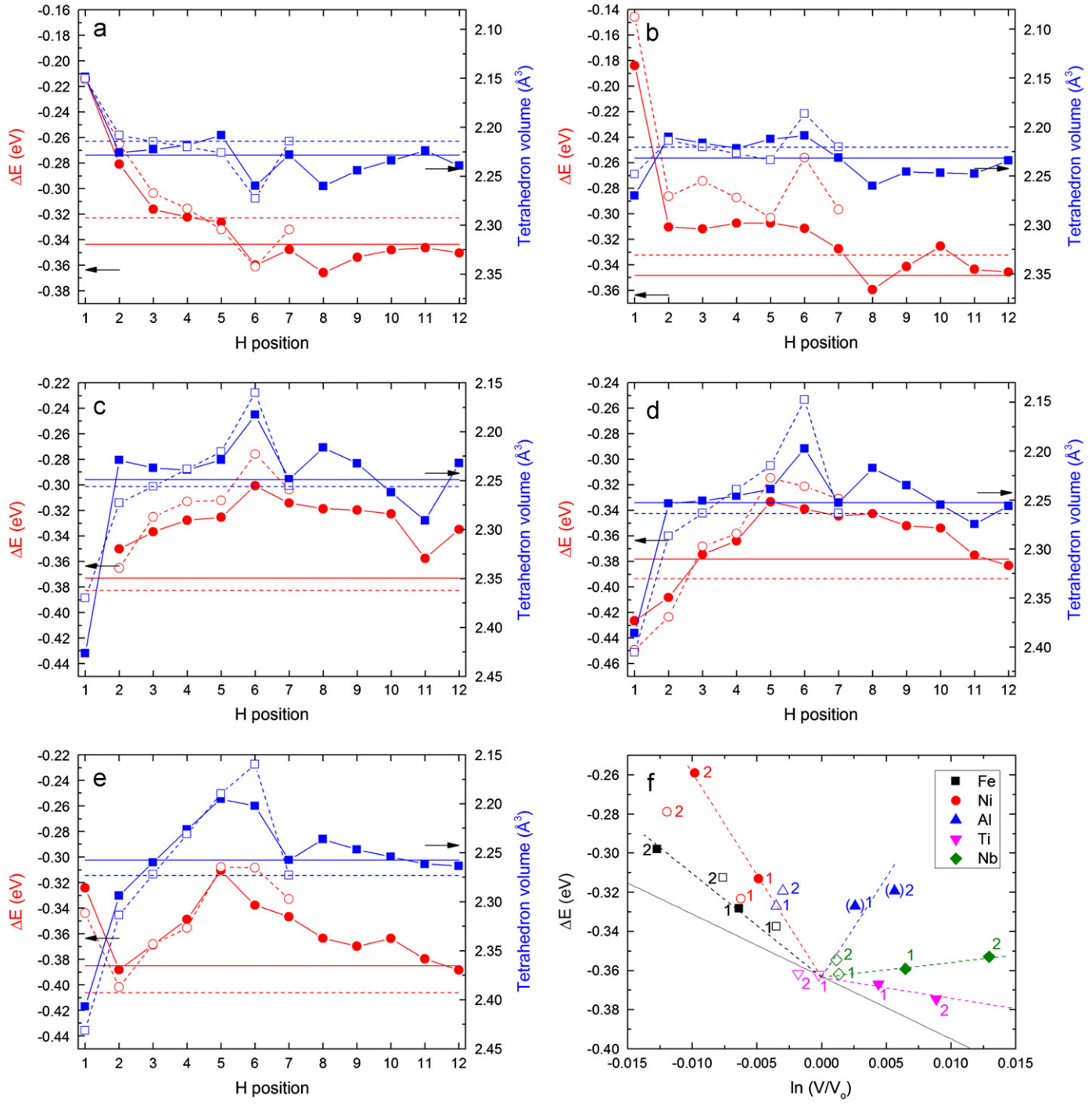

Fig. 2. Site energies and tetrahedron volume at 12 different H positions in $V_{53}X_1$ and 7 H positions in $V_{52}X_2$: (a) Fe, (b) Ni, (c) Al, (d) Ti, and (e) Nb. The blue and red horizontal lines represent the average tetrahedron volume and the estimated site energy, respectively. The solid lines and the solid symbols are for $V_{53}X_1$, and the dashed lines and the open symbols are for $V_{52}X_2$. The black arrows indicate the values of V_{54}. Note that the tetrahedron volume decreases from the bottom to the top. In (f), solid symbols represent the averaged total site energy and the open symbols represent the averaged V_4 site energy. The black solid line indicates the value of pure V in Fig. 1, and the dashed lines are a guide to the eye. The annotations indicate the number of X atoms in the supercell. (For interpretation of the references to color in this figure legend, the reader is referred to the web version of this article.)

3.3. *High alloy concentration*

Here, we examine the electronic effect at higher concentrations, $V_{48}X_6$ and $V_{42}X_{12}$. In practice, major alloying elements are added in 10–20 at% to bring a sizeable effect to durability [2,5,33]. Note that the alloying elements investigated here show significant maximum solubility in vanadium (54 at% for Al) or even form complete solid solutions (Ti, Fe, and Nb) at high temperatures, except for Ni, which shows a maximum solubility of 24 at% [34]. However, the solubility decreases significantly as the temperature decreases and intermediate phases, such as V_3Ni, V_3Al, and the σ phase in V–Fe, form. Here, the simulated high concentration cases assume supersaturated alloys.

3.3.1. *Electronic structure*

Before providing the detailed analysis on the electronic structure, we first attempt to correlate the electronegativity of the

alloying elements with the site energy sequence determined in Section 3.2.2. The electronegativity follows the sequence Ti (1.54) < Nb (1.6) ~ Al (1.61) ~ V (1.63) < Fe (1.83) < Ni (1.91) < H (2.20), which is largely consistent with the sequence in the average site energy, except for Al. More electropositive elements seemingly reduce the site energy. To better understand this behavior, we analyze the *d*-band filling because it is a critical factor that affects the interaction with hydrogen atoms [35]. In Fig. 3, the shaded region shows the projected density of states (PDOS) to orthonormalized *d*-orbitals. The position of the *d*-band center (ε_d) relative to the Fermi energy (ε_F), $\varepsilon_d - \varepsilon_F$, has the following sequence—Ti (1.14) > V (1.02) ~ Nb (1.02) > Al (0.79) > Fe (0.45) > Ni (0.10). The overall *d*-band shape remains largely unchanged in the case of Nb and Ti, except for a slight shift of the *d*-band center. Nb is almost neutral in terms of the electronic effect. Except for Al, the sequence of $\varepsilon_d - \varepsilon_F$ exactly matches with the site energy sequence of the V_4 sites in Fig. 2f.

A closer look into the repulsion by Al is required, and for this purpose, we choose a H6 configuration in the $V_{42}Al_{12}$ structure, where H is trapped in the V_3Al site. Fig. 4a and b shows the PDOS of H and the four nearest metal atoms for V_{54} and $V_{42}Al_{12}$, respectively. The isolated lowest energy state is introduced by the H interstitial. In V_{54}, the PDOS of H is well contained in this lowest energy state, but in $V_{42}Al_{12}$, it is more dispersed to the states at higher energy. The notable difference is the reduced PDOS of the nearby V atoms. However, the contribution by Al appears to be greater. In Fig. 3, one can observe that the total DOS of $V_{42}Al_{12}$ is extended toward lower energy compared to the other

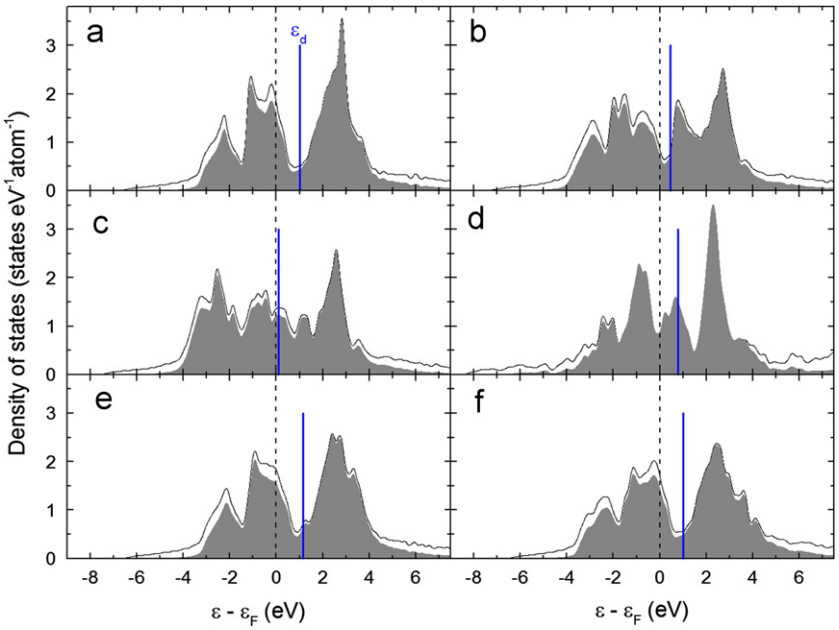

Fig. 3. Density of states in $V_{42}X_{12}$: (a) pure V, (b) Fe, (c) Ni, (d) Al, (e) Ti, and (f) Nb. The solid black lines are total DOS, and the gray area is the PDOS of the *d*-orbitals. The blue lines indicate the position of the *d*-band center. (For interpretation of the references to color in this figure legend, the reader is referred to the web version of this article.)

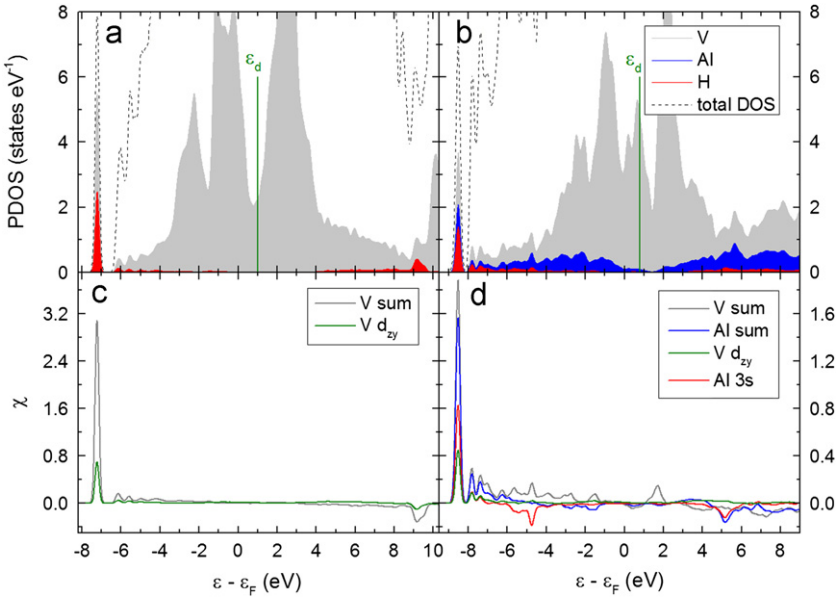

Fig. 4. Projected density of states and orbital overlap in V_{54} and $V_{42}Al_{12}$. PDOS of the H atom and its four nearest metal atoms are shown for (a) V_{54} and (b) $V_{42}Al_{12}$. Orbital overlap between H 1*s* orbital and the atomic orbitals of one of the nearest V or Al is shown for (c) V_{54} and (d) $V_{42}Al_{12}$. V sum and Al sum are the summation over all of the orbitals that belong to V or Al. Note that the ordinate scale in (d) is half the scale in (c).

transition metal elements. These low-energy states from Al strongly hybridize with the H 1*s* orbital, and consequently, the state introduced by hydrogen is formed at a relatively lower energy. To quantify the contribution from each orbital, we plot the energy-resolved orbital overlap:

$$\chi_{lm}(\varepsilon) = 1/N_k \sum_{n,\mathbf{k}} \langle \phi_l | \psi_{n\mathbf{k}} \rangle \langle \psi_{n\mathbf{k}} | \phi_m \rangle \delta(\varepsilon - \varepsilon_{n\mathbf{k}}), \quad (4)$$

where ϕ are atomic orbitals; N_k is the total number of k points; $\psi_{n\mathbf{k}}$ and $\varepsilon_{n\mathbf{k}}$ are the nth Bloch function and the eigen-energy at the $\mathbf{k}$ vector, respectively. A Gaussian broadening of 0.01 Ry is used for $\delta(\varepsilon - \varepsilon_{n\mathbf{k}})$. When $l=m$, this is the PDOS of the atomic orbital ϕ_l. When $l \neq m$, a positive sign of $\chi_{lm}(\varepsilon)$ indicates a bonding interaction, whereas a negative sign represents an antibonding interaction; the absolute value corresponds to the magnitude of the interaction. Here, ϕ_l is fixed to the 1*s* orbital of H, and the overlaps with the orbitals of V or Al are shown in Fig. 4c and d. In V_{54}, the bonding interaction is localized in the lowest energy state, and the antibonding interaction is located well above ε_F. In $V_{42}Al_{12}$, the bonding state is shifted to lower energy; however, the antibonding state is also shifted to lower energy, especially with the Al 3*s* orbital, which exhibits significant antibonding contributions below ε_F. In addition, stronger hybridization with Al causes weaker hybridization with the V *d*-orbitals, as can be observed in the much smaller overlap with d_{zy}. Consequently, H avoids the energetically unfavorable interaction with Al and prefers to be exclusively surrounded by V.

3.3.2. Coordination

Another interesting characteristic of the V alloy is the variation in its coordination environment. Fig. 5a and b shows the final atomic positions when H is placed at the H1 position in $V_{48}Ni_6$ and the H2 position in $V_{48}Al_6$, respectively. The hydrogen position significantly deviates from the original tetrahedral site (labeled as the *T* site); in Ni, it moves to an octahedral site (labeled as the *O* site), which has a Ni vertex at its short diagonal (length of *a*, lattice parameter), whereas in Al, it sits between two tetrahedral sites and has five metal atoms surrounding it. We name this site the *P* site, as shown in Fig. 5c. Even before inserting a hydrogen atom, the electrostatic potential map provides a rough idea about the preferred site. Fig. 6 compares the case of pure vanadium with that of $V_{48}Ni_6$. The contour map cuts the H1 position, which is the V_3Ni_1 site. In pure V (Fig. 6a), the *T* site is located at the distinct maximum that is energetically well separated from the nearby *O* site. However, in $V_{48}Ni_6$ (Fig. 6b), the potential difference between the *O* and *T* sites becomes very small and the position is shifted toward the *O* site at the center. This result indicates the strong stabilization of the *O* site in the presence of a Ni atom.

The change in coordination environment upon alloying certainly relies on the electronic effect and is indeed intriguing. This change is worth further investigation because it could affect the formation of V_2H, where the H atoms preferentially sit at the *O* sites [36].

3.3.3. Site energy

The site energies are calculated and summarized in Fig. 7. As mentioned above, some H atoms move to the *O* or *P* site, or other *T* sites (see the annotations in Fig. 7). The general trend in the site energy is Ti < Nb < Al < Fe < Ni in the case of $V_{48}X_6$. From Ti to Nb, the electronic contribution is stronger such that the site energy in V–Ti is always lower than that in V–Nb. From Al to Fe, the elastic effect overtakes the electronic effect due to their large size difference (see Fig. S3), and some stable sites in Al now

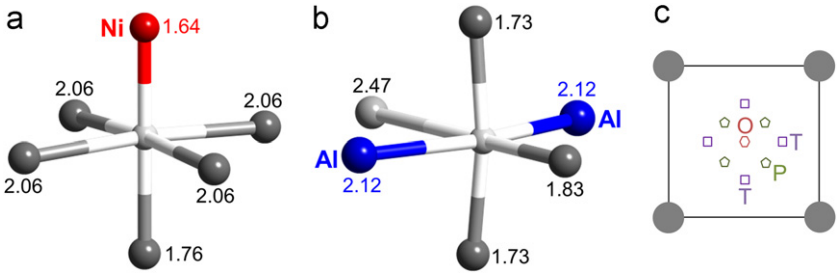

Fig. 5. Metal atom coordination around H: (a) H1 position in $V_{48}Ni_6$, (b) H2 position in $V_{48}Al_6$, and (c) schematic diagram to show the position of the T, O, and P sites on the (001) plane of vanadium. The atoms are drawn in different colors: H, V, Ni, and Al in white, gray, red, and blue, respectively. The numbers on each metal atom are the distance from H in Å. (For interpretation of the references to color in this figure legend, the reader is referred to the web version of this article.)

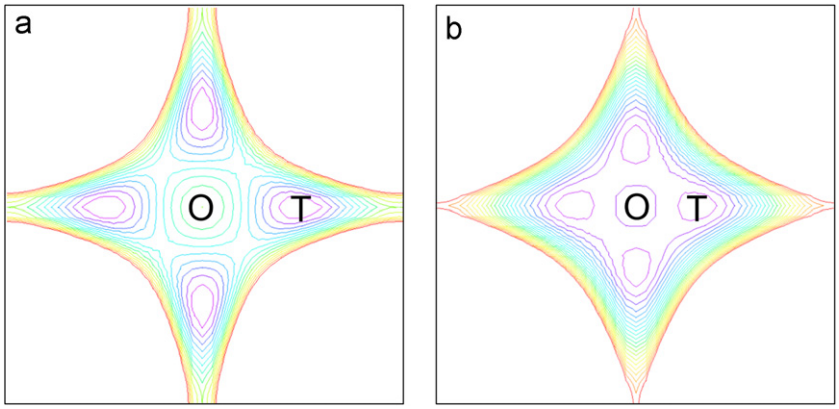

Fig. 6. Contour map of electrostatic potential for (a) pure V and (b) $V_{48}Ni_6$. The plane cut is orthogonal to the [001] direction and is taken where the electrostatic potential at the *T* site reaches a maximum. The *T* site in (b) corresponds to the H1 position. The potential increases as the color changes from red to purple. The color is not correlated to the absolute value of the electrostatic potential. The white regions at the corners have an even lower potential. The isopotential lines are drawn in an interval of 0.068 V. (For interpretation of the references to color in this figure legend, the reader is referred to the web version of this article.)

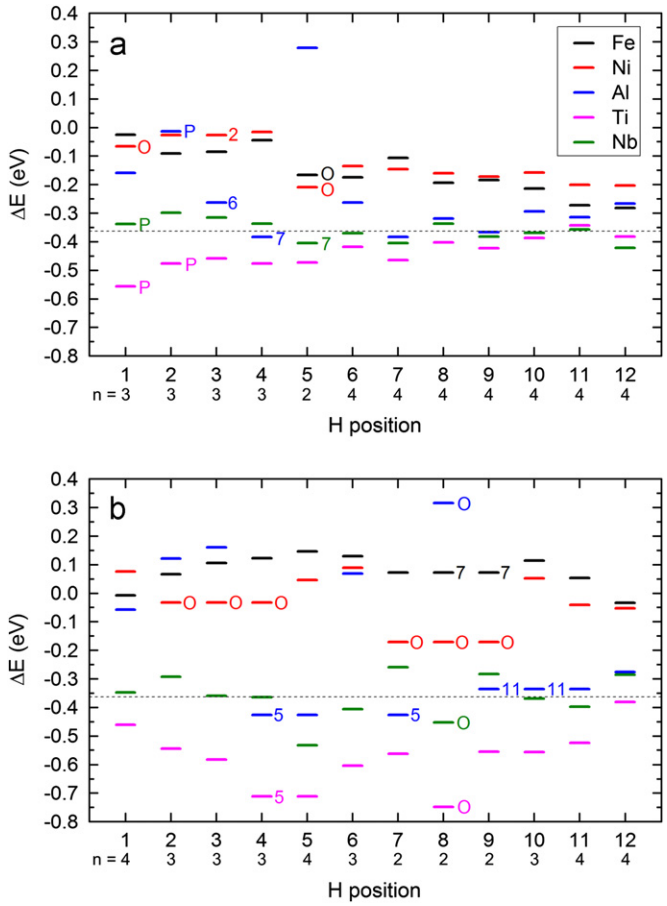

Fig. 7. Site energies at 12 different H positions: (a) $V_{48}X_6$ and (b) $V_{42}X_{12}$. Numbers in smaller font below the bottom label represent the coordination (V_nX_{4-n}) for each *T* site. The annotations (O, P, or H position index) indicate the final stable site when the final site is different from the initial *T* site. The black dotted lines show the ΔE of pure V.

become more stable than those in Fe. It is consistently observed that H cannot sit next to Al unless the unfavorable *T* site (V_nAl_{4-n} where $n \neq 4$) is exclusively connected to other unfavorable *T* sites. To elaborate, each *T* site has four nearest *T* sites. For example, an H1 site has three H1 and one H2 sites as its nearest neighbors (refer to the neighboring *T* sites in Table 2 and the diagram in Fig. S2), and therefore, the hydrogen at the H1 site in $V_{48}X_6$ cannot escape from the V_3Al_1 position because the H2 site is also a V_3Al_1 site.

At higher alloy concentrations, i.e., the $V_{42}X_{12}$ structure, the site energies in Ni become lower than those in Fe. The reasons can be attributed to both the electronic and elastic contributions: (i) Ni creates some stable *O* sites that attract nearby H atoms, and (ii) the volume difference becomes larger, which favors Ni. It is interesting to observe that the two most stable sites in $V_{42}Ni_{12}$ are the *O* sites. One can observe that even for Ti and Nb, the V_2X_2 H8 position is unstable and the H atom moves to the *O* site. The final *O* sites for larger atoms (Al, Ti, and Nb), however, are different from those in Ni: two V atoms sit at the vertices of the short diagonal and four X atoms sit at the vertices of the long diagonals (length of $\sqrt{2}a$) of the octahedron, whereas the opposite happens in the case of Ni. Irrespective of the composition and alloying element, all of the V_4 sites remain stable. In summary, at high concentrations, we expect to see several types of metal coordinations around the H site depending on the local arrangements of the alloying atoms, and we may observe changes in the solubility sequence due to enlarged electronic or elastic effects.

3.4. Statistical analysis using special quasi-random structure

The cases of $V_{48}X_6$ and $V_{42}X_{12}$ provide us insights about the characteristics of each alloying element. The artificial symmetry, however, cannot provide a realistic environment of a random alloy. For example, the probabilities of each site, $p(V_4)=0.259$ (0.366), $p(V_3X_1)=0.593$ (0.418), $p(V_2X_2)=0.148$ (0.179), $p(V_1X_3)=0.000$ (0.034), and $p(X_4)=0.000$ (0.002), significantly deviate from the ideal value written inside the parentheses. Using a SQS of the bcc alloy [27] for $V_{12}X_4$, we calculate the site energies of the 96 possible H sites (48 independent sites). This structure more closely reflects a random arrangement: $p(V_4)=0.333$ (0.316), $p(V_3X_1)=0.375$ (0.422), $p(V_2X_2)=0.250$ (0.211), $p(V_1X_3)=0.042$ (0.047), and $p(X_4)=0$ (0.004). Table 3 summarizes the number of stable sites for different coordination environments. There are two types of V_2X_2: one with two X atoms at the short edge (length of $(\sqrt{3}/2)a$, labeled as V_2X_2–*s*) of a tetrahedron and the other at the long edge (length of *a*, labeled as V_2X_2–*l*). In many cases, the H atoms sit between the ideal *T* and *O* sites, and an *O* site is assigned when $d_T > d_O + 0.5$ Å, where d_T and d_O are the distance from the ideal tetrahedral and octahedral positions, respectively. The *T*–*O* distance in pure vanadium is 0.75 Å. Within this criterion, all of the octahedral occupations exhibit an almost linear M–H–M arrangement along its short diagonal.

In the case of Ni, the number of stable interstitial sites is significantly reduced from 96 to 69. The preference for the *O* site clearly appears: whenever two Ni atoms form a long edge, the H atom wants to sit between them, i.e., all V_2X_2-l and V_1X_3 sites are unstable, and these 12 *T* sites collapse into the three most stable *O* sites (see Table 3). The most noteworthy change in the number of stable sites is observed in Al due to the strong repulsion. The average site energies are summarized in Table 4.

3.4.1. Hydrogen distribution at finite temperature

To estimate the site energy as a function of concentration at finite temperature, we perform Monte Carlo simulations using the Metropolis algorithm. For the site energies, the concentration is varied from 1 to 16 H atoms per $V_{12}X_4$ simulation cell. The final values are averages from the last 10^7 steps in a total of 2×10^7 simulation steps. To arrange multiple H atoms, the interaction between H atoms must be explicitly considered. For simplicity, we assume a complete blocking within half of the lattice parameter, ca.

Table 3
Number of final stable sites in the $V_{12}X_4$ configuration after structure optimization. The numbers inside the parentheses are the initial numbers. In V_2X_2, the first number and the second number correspond to V_2X_2-s (short edge) and V_2X_2–*l* (long edge), respectively.

	V_4 (32)	V_3X_1 (36)	V_2X_2 (16, 8)	V_1X_3 (4)	*T* (96)	*O* (0)	*P* (0)	Total (96)
Fe	32	34	12, 0	0	78	3	2	83
Ni	32	24	8, 0	0	64	3	2	69
Al	32	12	4, 2	0	50	0	3	53
Ti	26	30	14, 4	4	78	0	2	80
Nb	32	34	16, 2	4	88	0	0	88

Table 4
Average site energy for each type of interstitial position in the $V_{12}X_4$ configuration. Units are in eV.

	V_4	V_3X_1	V_2X_2–*s*	V_2X_2–*l*	V_1X_3	*O*	*P*
Fe	0.020	0.147	0.133	–	–	0.099	0.093
Ni	−0.016	0.081	0.126	–	–	−0.115	0.000
Al	−0.273	0.038	0.239	0.375	–	–	0.291
Ti	−0.312	−0.381	−0.465	−0.416	−0.512	–	−0.470
Nb	−0.350	−0.325	−0.273	−0.278	−0.165	–	–

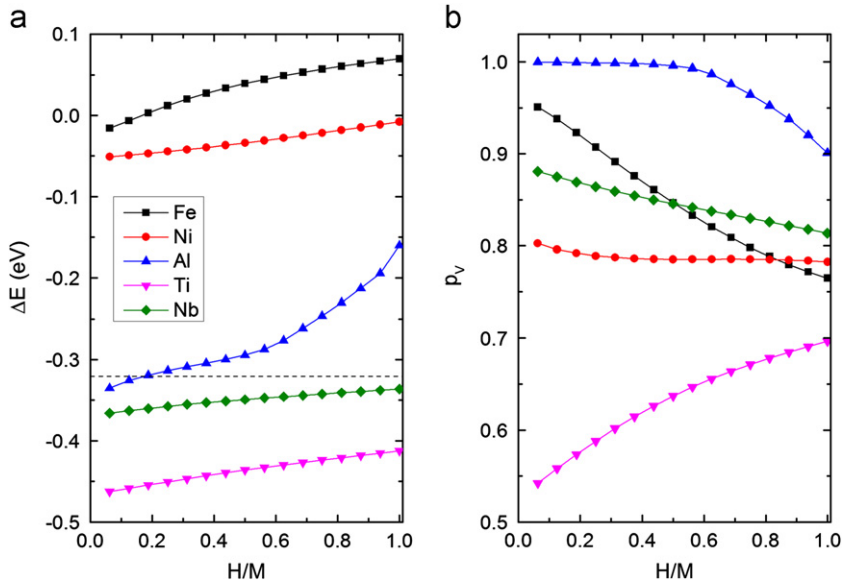

Fig. 8. (a) Site energy per H atom and (b) p_V as a function of H/M in $V_{12}X_4$ at 673 K. The dashed line in (a) indicates the site energy in V_{16}.

1.5 Å, which corresponds to the blocking of the six nearby *T* sites and two *O* sites in the case of a *T* site occupation [37].

Fig. 8a shows the site energy per H atom at 673 K. Note that the site energy in V_{16} (dashed line) is different from that in 54-atom cell because the cell size is not sufficient to obtain a fully converged value. The site energy sequence among the X atoms is the following: Ti < Nb < Al < Ni < Fe. The result also confirms that the site energy in Ni is smaller than that in Fe at high alloy concentrations, and the apparent site energy in Al is quite small (even smaller than that in V_{16} at low concentration) due to the elastic effect. However, the rapid increase at high concentrations ($H/M > 0.5$) appears to be related to the limited number of stable V_4 sites. To better understand this behavior, the probability of having vanadium as the nearest neighbor (p_V) is calculated and plotted in Fig. 8b. Indeed, the steep increase in ΔE accompanies a decrease in p_V. As H/M increases, the V_4 sites cannot accommodate all of the H atoms and they are forced to occupy the V_nAl_{4-n} sites ($n \neq 4$) that have considerably higher site energy (see Table 4), which simultaneously decreases p_V and increases ΔE. An increase in ΔE and a decrease in p_V is commonly observed for Fe, Ni, and Nb, but they exhibit a more gradual change because the energy difference between the different types of sites is not as large as in Al (see Table 4). Except for Ti, all of the other cases show preference for V because p_V lies above the ideal value of 0.75. The ΔE and p_V in Ti exhibit the opposite trend because more H atoms are forced to sit near V as H/M increases (the V_4 site is the least favored), which is the exact opposite of the Al case.

3.4.2. Configurational entropy

A thermodynamic quantity that is linked to the site preference appearing in the variation in p_V is configurational entropy. In fact, estimating the entropy is a more involved process. To explore all of the possible configurations with the correct probabilities, the required number of simulation steps rapidly increases with the number of H atoms. Here, the number of H atoms is limited to 4, and 10^8 simulation steps are used for the same simulation conditions as in the previous section. The following unitless quantity is used as a measure of the configurational entropy:

$$\sigma_c = -\sum_i P_i \ln P_i, \quad (5)$$

where P_i is the probability of the *i*th distinct configuration. The absolute σ_c value does not correspond to the experimental configurational entropy because of the size limitation and approximations imposed in our simulation, but it will provide a sense of the relative magnitude for different alloy systems. The results are summarized in Fig. 9. For comparison, the maximum σ_c is calculated based on the condition of no blocking and identical site energies for all of the *T* sites (labeled as bn-0). The upper bound for the six blocking *T* sites is also obtained assuming identical site energy (labeled as bn-6). As expected, the drop in σ_c is the most pronounced in Al, and the values are approximately 60% of those of bn-6. The value is the largest in Nb. Although the smallest or largest σ_c arises from the X that has the smallest or largest number of stable sites (Table 3), the detailed sequence does not follow that of the total number of stable sites. Especially when $H/M = 0.0625$ (one H atom), σ_c of Fe is the second smallest, whereas its total number of stable sites is the second largest. Such a variation originates from the site energy distribution, and we can infer that Fe has smaller number of stable sites within the

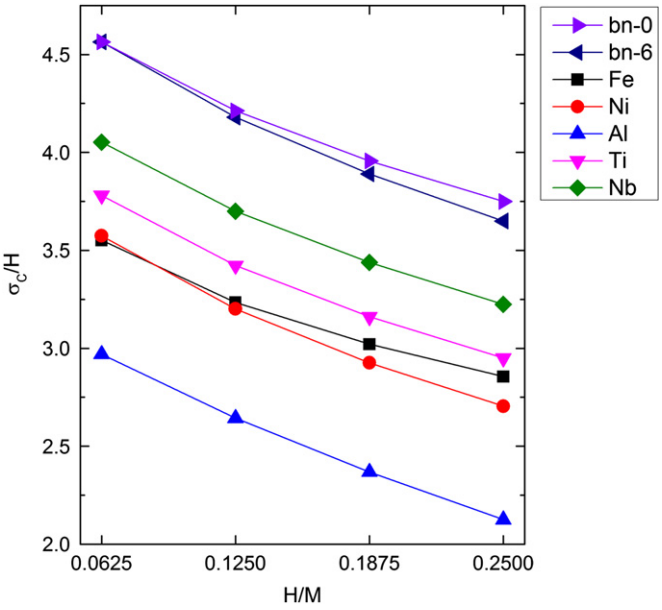

Fig. 9. Measure of configurational entropy per H atom as a function of H/M at 673 K. The right triangle in violet (bn-0) is the upper bound. (For interpretation of the references to color in this figure legend, the reader is referred to the web version of this article.)

energy window covered by the thermal energy at 673 K, compared to the other X atoms.

In summary, although the strong repulsion of H by Al may not be detected in the measurement of enthalpy, this effect should clearly appear in the measurement of entropy. The element in the same group, Nb, appears to be the best in preserving the effective number of H interstitial sites. In relation to the effect on permeability, the σ_c values can also be connected to hydrogen diffusivity in the alloy. Very small σ_c values at low H/M ratios may indicate the existence of trapping centers, whose site energies are separated from those of other sites. For example, in V–Al, the H atoms would diffuse mostly thorough the V_4 sites, and the loss of connection between the V_4 sites results in trapping of H in the V_4 sites. Therefore, if the site energies are similar, the alloy system that has the larger σ_c would be beneficial for permeability applications.

Here, we limit ourselves to the discussion of metal–hydrogen interactions in static configurations and the solubility of hydrogen. Calculations on the diffusivity of hydrogen should follow to predict the permeability of a membrane. However, higher permeability does not necessarily promise better overall performance in V alloy membranes. For instance, if the diffusivity does not considerably differ, the V–Ti membrane may have the highest permeability, but even more serious embrittlement may result from the increased H solubility [2]. In this respect, we deem that further investigation on metal–hydrogen interactions, such as strong local attraction/repulsion, site preference changes, or formation of hydrides, in relation to H-induced embrittlement is as important as the prediction on permeability and is a subject of future work.

4. Conclusions

We have investigated the alloying effect on hydrogen insertion in view of elastic and electronic contributions in vanadium alloyed with Fe, Ni, Al, Ti, and Nb. At low alloying concentrations, the elastic effect is extrapolated from that in pure V, and the electronic effect is isolated. The overall sequence of the electronic contribution in H affinity at low alloying concentration is Ti > Nb > Fe > Ni > Al. Al exhibits the strongest repulsion and cannot accommodate hydrogen in its nearest interstitial sites. As the alloying concentration increases, a coordination change around the H atoms is predicted in some cases. Specifically, Ni strongly stabilizes the *O* sites, and this effect combined with the enhanced elastic effect makes Ni more favorable than Fe for H insertion. At $x_X=0.25$, the strong repulsion by Al is not evident in the site energy due to the significant elastic contribution, but a large drop in configurational entropy is predicted due to the reduced number of stable sites. Regarding the design of a vanadium alloy membrane, if one intends to decrease the hydrogen solubility to mitigate the embrittlement problem, smaller alloying elements will be more effective, especially when they form solid solutions with vanadium in a wide composition range. For hydrogen diffusion, alloying elements that do not induce a strong variation in site energies can be a good candidate because mobile hydrogen will not be trapped or blocked by the sites that have very low or high energy. The short-range metal–hydrogen interactions discussed here could alter the stability of hydrides or induce rearrangement of metal atoms [38], thereby affecting the performance of the membrane; therefore, these interactions require further attention.

Acknowledgments

This work was supported by Korea Institute of Science and Technology (Grant no. 2E22742).

Appendix A. Supporting information

Supplementary data associated with this article can be found in the online version at http://dx.doi.org/10.1016/j.memsci.2012.08.034.

References

[1] S. Adhikari, S. Fernando, Hydrogen membrane separation techniques, Ind. Eng. Chem. Res. 45 (2006) 875–881.
[2] M.D. Dolan, Non-Pd BCC alloy membranes for industrial hydrogen separation, J. Membr. Sci. 362 (2010) 12–28.
[3] M. Amano, M. Komaki, C. Nishimura, Hydrogen permeation characteristics of palladium-plated V–Ni alloy membranes, J. Less Common Met. 172–174 (1991) 727–731.
[4] Y. Zhang, T. Ozaki, M. Komaki, C. Nishimura, Hydrogen permeation characteristics of vanadium–aluminium alloys, Scripta Mater. 47 (2002) 601–606.
[5] S.N. Paglieri, J.R. Wermer, R.E. Buxbaum, M.V. Ciocco, B.H. Howard, B.D. Morreale, Development of membranes for hydrogen separation: Pd coated V–10Pd, Energy Mater.: Mater. Sci. Eng. Energy Syst. 3 (2008) 169–176.
[6] N. Watanabe, H. Yukawa, T. Nambu, Y. Matsumoto, G.X. Zhang, M. Morinaga, Alloying effects of Ru and W on the resistance to hydrogen embrittlement and hydrogen permeability of niobium, J. Alloys Compd. 477 (2009) 851–854.
[7] C. Nishimura, M. Komaki, S. Hwang, M. Amano, V–Ni alloy membranes for hydrogen purification, J. Alloys Compd. 330–332 (2002) 902–906.
[8] M.D. Dolan, K.G. McLennan, J.D. Way, Diffusion of atomic hydrogen through V–Ni alloy membranes under nondilute conditions, J. Phys. Chem. C 116 (2012) 1512–1518.
[9] H. Yukawa, D. Yamashita, S. Ito, M. Morinaga, S. Yamaguchi, Compositional dependence of hydriding properties of vanadium alloys at low hydrogen pressures, J. Alloys Compd. (2003) 45–49 356–357.
[10] M. Gupta, R.P. Gupta, D.J. Singh, Origin of the anomalous absence of hydride formation by $ZrPd_2$, Phys. Rev. Lett. 95 (2005) 056403.
[11] E. Veleckis, R.K. Edwards, Thermodynamic properties in the systems vanadium–hydrogen, niobium–hydrogen, and tantalum–hydrogen, J. Phys. Chem. 73 (1969) 683–692.
[12] J.F. Lynch, J.J. Reilly, F. Millot, The absorption of hydrogen by binary vanadium–chromium alloys, J. Phys. Chem. Solids 39 (1978) 883–890.
[13] O.J. Kleppa, P. Dantzer, M.E. Melnichak, High-temperature thermodynamics of the solid solutions of hydrogen in bcc vanadium, niobium, and tantalum, J. Chem. Phys. 61 (1974) 4048–4058.
[14] R. Hempelmann, D. Richter, J.J. Rush, J.M. Rowe, Hydrogen site distribution in the alloy system $NB_{100-x}V_xH_y$ studied by neutron vibrational spectroscopy, J. Less Common Met. 172–174 (1991) 281–292.
[15] R.C. Brouwer, R. Griessen, Heat of solution and site energies of hydrogen in disordered transition-metal alloys, Phys. Rev. B 40 (1989) 1481–1494.
[16] R.C. Brouwer, E. Salomons, R. Griessen, Diffusion of hydrogen in $Nb_{1-y}V_y$ alloys, Phys. Rev. B 38 (1988) 10217–10226.
[17] R.C. Brouwer, J. Rector, N. Koeman, R. Griessen, Hydrogen as a local probe—diffusion and short-range order in $Ti_{1-y}V_y$ alloys, Phys. Rev. B 40 (1989) 3546–3559.
[18] K. Watanabe, Y. Fukai, Calorimetric studies of the behavior of hydrogen in vanadium and vanadium alloys, J. Phys. Soc. Jpn. 54 (1985) 3415–3424.
[19] P. Kamakoti, B.D. Morreale, M.V. Ciocco, B.H. Howard, R.P. Killmeyer, A.V. Cugini, D.S. Sholl, Prediction of hydrogen flux through sulfur-tolerant binary alloy membranes, Science 307 (2005) 569–573.
[20] P. Kamakoti, D.S. Sholl, Ab initio lattice-gas modeling of interstitial hydrogen diffusion in CuPd alloys, Phys. Rev. B 71 (2005) 014301.
[21] O.M. Løvvik, R.A. Olsen, Density functional calculations on hydrogen in palladium–silver alloys, J. Alloys Compd. 330–332 (2002) 332–337.
[22] C.G. Sonwane, J. Wilcox, Y.H. Ma, Achieving optimum hydrogen permeability in PdAg and PdAu alloys, J. Chem. Phys. 125 (2006) 184714.
[23] X.Z. Ke, G.J. Kramer, O.M. Løvvik, The influence of electronic structure on hydrogen absorption in palladium alloys, J. Phys.: Condens. Matter 16 (2004) 6267–6277.
[24] S. Aboud, J. Wilcox, A density functional theory study of the charge state of hydrogen in metal hydrides, J. Phys. Chem. C 114 (2010) 10978–10985.
[25] J.P. Perdew, K. Burke, M. Ernzerhof, Generalized gradient approximation made simple, Phys. Rev. Lett. 77 (1996) 3865–3868.
[26] P. Giannozzi, S. Baroni, QUANTUM ESPRESSO: a modular and open-source software project for quantum simulations of materials, J. Phys.: Condens. Matter 21 (2009) 395502.
[27] C. Jiang, C. Wolverton, J. Sofo, L.Q. Chen, Z.K. Liu, First-principles study of binary bcc alloys using special quasirandom structures, Phys. Rev. B 69 (2004) 214202.
[28] T. Kuji, W.A. Oates, Thermodynamic properties of Nb–H alloys I: the α phase, J. Less Common Met. 102 (1984) 251–260.
[29] R. Feenstra, R. Griessen, D.G. Degroot, Hydrogen induced lattice expansion and effective H–H interaction in single-phase PdH_c, J. Phys. F—Met. Phys. 16 (1986) 1933–1952.
[30] Z. Jenei, H.P. Liermann, H. Cynn, J.H.P. Klepeis, B.J. Baer, W.J. Evans, Structural phase transition in vanadium at high pressure and high temperature: influence of nonhydrostatic conditions, Phys. Rev. B 83 (2011) 054101.

[31] L. Koči, Y. Ma, A.R. Oganov, P. Souvatzis, R. Ahuja, Elasticity of the superconducting metals V, Nb, Ta, Mo, and W at high pressure, Phys. Rev. B 77 (2008) 214101.
[32] A.J. Maeland, Investigation of the vanadium–hydrogen system by X-ray diffraction techniques, J. Phys. Chem. 68 (1964) 2197–2200.
[33] M.D. Dolan, G. Song, D. Liang, M.E. Kellam, D. Chandra, J.H. Lamb, Hydrogen transport through $V_{85}Ni_{10}M_5$ alloy membranes, J. Membr. Sci. 373 (2011) 14–19.
[34] H. Okamoto, Desk Handbook: Phase Diagrams for Binay Alloys, ASM International, Materials Park, Ohio, 2000.
[35] H. Smithson, C.A. Marianetti, D. Morgan, A. Van der Ven, A. Predith, G. Ceder, First-principles study of the stability and electronic structure of metal hydrides, Phys. Rev. B 66 (2002) 144107.
[36] Y. Noda, K. Masumoto, S. Koike, T. Suzuki, S. Sato, X-ray crystallographic study of tetragonal and monoclinic β_1-V_2H, Acta Crystallogr. B—Struct. Sci. 42 (1986) 529–533.
[37] G. Boureau, A simple method of calculation of the configurational entropy for interstitial solutions with short-range repulsive interactions, J. Phys. Chem. Solids 42 (1981) 743–748.
[38] J. Bloch, O. Levy, B. Pejova, J. Jacob, S. Curtarolo, B. Hjörvarsson, Prediction and hydrogen acceleration of ordering in iron–vanadium alloys, Phys. Rev. Lett. 108 (2012) 215503.